Article

Not peer-reviewed version

Sandstone as a Sustainable Alternative to Shield Photons

Gabrielli Wisniewski Pietralla , Isonel S. Meneguzzo , Luiz F. Pires *

Posted Date: 23 June 2025

doi: 10.20944/preprints202506.1819.v1

Keywords: radiation shielding; mean free path; linear attenuation coefficient; mass attenuation coefficient; sandstone; energy buildup factor; exposure buildup factor; buildup factor

 doi:10.20944/preprints202506.1819.v1

Article

Sandstone as a Sustainable Alternative to Shield Photons

Gabrielli Pietralla [1], Isonel S. Meneguzzo [2] and Luiz F. Pires [1,*]

[1] Laboratory of Physics Applied to Soils and Environmental Sciences, Departament of Physics, State University of Ponta Grossa, Ponta Grossa CEP 84.030-900, Paraná, Brazil

[2] Department of Geosciences, State University of Ponta Grossa, Ponta Grossa CEP 84.030-900, Paraná, Brazil

* Correspondence: lfpires@uepg.br; Tel.: +55-42-32203044

Abstract

The materials typically used for radiation shielding include lead, concrete, and polymers. However, some of these materials can be toxic or very expensive to produce. This raises interest in using more readily available natural materials, such as rocks, as an alternative. In this study, we analyze the radiation shielding efficiency of sandstones. We evaluated different layers of rock and obtained shielding parameters based on the composition of various oxides. The analysis revealed that these layers showed a predominance of silicon and aluminum oxides. Notably, the lowest photon energies (0.015 MeV and 0.1 MeV) displayed significant differences in photon attenuation, as indicated by linear and mass attenuation coefficients. This suggests that the chemical composition of the samples had a considerable impact on their shielding performance. Samples containing higher amounts of heavier elements proved to be more effective at attenuating radiation, efficiently reducing 50% (half-value layer) and 90% (tenth-value layer) of the photons. Additionally, the presence of these heavier elements decreased the production of secondary photons (buildup factor), further enhancing the samples' efficiency in shielding against radiation. Our results indicate that sandstones hold potential for radiation shielding, particularly when they contain higher quantities of heavier elements.

Keywords: radiation shielding; mean free path; linear attenuation coefficient; mass attenuation coefficient; sandstone; energy buildup factor; exposure buildup factor; buildup factor

1. Introduction

The use of radioactive sources in several applications, including medical imaging, radiation therapy, and industrial processes, necessitates the use of radiation shielding [1]. Various materials are used for this purpose, including lead, concrete, rocks, and polymers [2,3]. The most common are those with higher densities and composed of elements with high atomic numbers [4]. However, some of these materials, such as lead, are toxic, heavy, and expensive, and they can deteriorate over time. Therefore, it is crucial to explore alternative radiation shielding materials.

One of the issues facing Earth is the production of radioactive waste by the nuclear industry and power plants. One alternative for storing this waste is to construct underground bunkers [5]. Therefore, it is essential to find materials that can effectively shield against radiation, particularly photons. Rocks present an interesting alternative because they consist of materials with moderate atomic numbers [6,7]. Furthermore, they are abundant and less expensive compared to synthetic materials like polymers. Their widespread availability allows for the construction of remote facilities. Another advantage of using rocks is that they can be mixed with other materials to create composite materials for improved radiation shielding [8–10].

Gamma and X-ray photons are commonly produced by medical equipment or emitted by radioactive sources, such as those found in radioactive waste. Different photon energies require materials with varying characteristics [11]. In the case of rocks, their elemental composition is one of the fundamental factors affecting radiation shielding. Additionally, the rock's structure, which

 doi:10.20944/preprints202506.1819.v1

influences its density, is another crucial factor in determining shielding efficiency [12]. The presence of elements with higher atomic numbers enhances the material's effectiveness in shielding photons, which is the focus of the study presented here.

To understand how materials shield radiation, one of the first parameters to calculate is the linear attenuation coefficient (LAC). However, since the LAC depends on the density of materials, the mass attenuation coefficient (MAC) is more useful for comparing materials with different densities [13]. Other important parameters include the mean free path (MFP), the half-value layer (HVL), and the tenth-value layer (TVL). These parameters are crucial for understanding how photons interact with matter. For example, the HVL and TVL indicate the thicknesses of materials required to attenuate 50% and 90% of photons, respectively [14].

In addition to these parameters, two important factors for quantifying the complex interactions of photons with matter are the energy buildup factor (EBF) and the exposure buildup factor (EABF). The EBF is defined as the ratio of the total photon energy fluence—comprising both primary and scattered photons—to the primary photon energy fluence at a specific point within a shielding material. Meanwhile, the EABF represents the ratio of total exposure, which includes both primary and scattered photons, to the exposure due to primary photons alone at that same point within the shielding material [15]. In practical terms, the EBF indicates how much the radiation dose increases due to secondary photons, while the EABF reflects the increase in exposure, illustrating the amount of ionization in the air caused by these photons.

Very few studies have investigated the radiation-shielding properties of sandstones. Since the composition of sandstones can vary by region, it is important to evaluate the radiation-shielding characteristics of these rocks locally. In this context, the findings of this study are unprecedented and contribute to the understanding of potential radiation-shielding materials. This research is based on the hypothesis that slight variations in the elemental composition of different sandstone layers significantly affect their shielding properties. The objectives of the study were as follows: 1) to determine the oxide content of sandstones from the same geological profile, 2) to examine how variations in the oxide composition of the samples impact the shielding parameters, 3) to identify the parameters that exhibit the most significant differences between the samples, and 4) to create reference data for selecting alternative materials for radiation shielding. All calculated shielding parameters were based on the elemental composition and densities of the rocks.

2. Materials and Methods

2.1. Study Area, Site Selection and Rocky Sampling

The study area consists of sandstones and diamictites from the Itararé Group (Carboniferous-Permian) located in the Paraná Sedimentary Basin in southern Brazil [16]. At the research site (UTM coordinates: 7181700 and 629590) (Figure 1), we observed diamictites, which are a mixture of sand and silt, along with layers of fine to medium sandstone. These sandstone layers belong to the Lagoa Azul Formation within the Itararé Group. Both the sandstones and diamictites exhibit signs of weathering, as evidenced by the presence of iron oxide veins. The rocks demonstrate vertical and sub-vertical fractures, while the sandstones display massive structures [17]. Additionally, the slope has a layer of young, residual soil at the top and has an incline of approximately 90 degrees.

 doi:10.20944/preprints202506.1819.v1

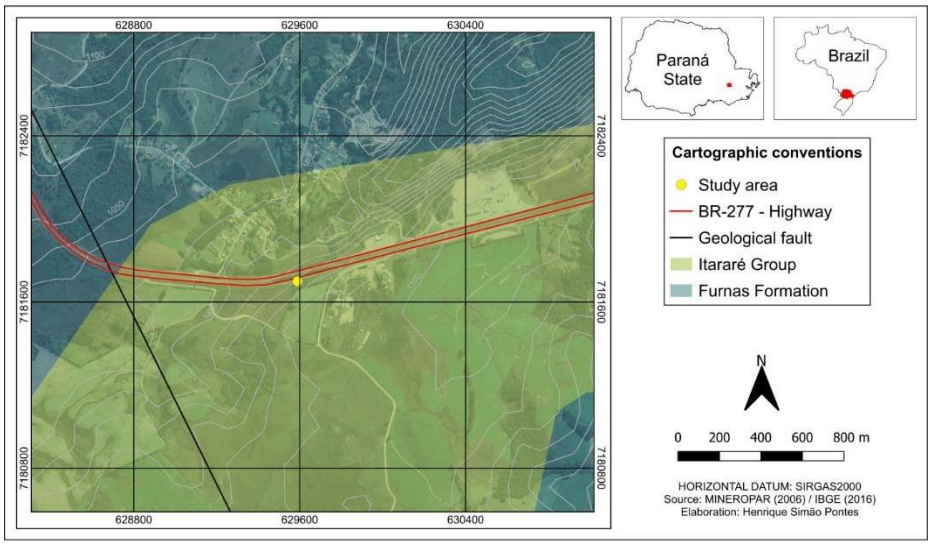

Figure 1. Map showing the region where the samples were collected in the Paraná State, Brazil.

The rock samples were collected at different depths using specific hammers and chisels for collecting geological material. The depths and definitions of the material collected were: 13.97 m (AR4), 14.02 m (RMPS), 14.12 m (RMPI), 14.23 m (RMPS), 14.32 m (AR2), and 15.50 m (AR1). The depths were defined from the top of the rock (Figure 2).

Figure 2. Photo showing the place where the rock samples were collected. The blue area represents where the samples were taken.

2.2. Chemical Composition of the Samples

The oxide composition of the rock samples was obtained using an energy-dispersive X-ray fluorescence spectrometer. The equipment used was the EDX-720 model (Shimadzu), which contains a Rhodium (Rh) tube. The voltage varies from 5 to 50 kV, and the operating current of the filament ranges from 1 to 1000 μA. The equipment's detection system consists of a Si(Li) semiconductor cooled with liquid nitrogen to -196 °C.

The measurements were carried out in triplicate (n=3), consisting of approximately 2 g of sample for each measurement. The samples were dried in an oven at 105 °C for 24 hours to remove residual moisture. Prior measurement, the samples were passed through a sieve with a mesh diameter of 2 mm and then reduced to a diameter of 45 μm by maceration using a mortar and pestle. These samples were placed in sample holders supplied by the equipment manufacturer and covered with Mylar film (6 μm thick).

The measurement time for each sample was 100 s in the Na-Sc (15 kV voltage) and Ti-U (50 kV voltage) energy ranges. The measurements were carried out under atmospheric pressure in a semi-

 doi:10.20944/preprints202506.1819.v1

quantitative mode. After the measurements, the data was obtained in the form of oxides as well as elements. However, only the data in oxide form was used to calculate the interaction parameters.

2.3. Radiation Shielding Parameters

The radiation shielding parameters were calculated using Phy-X PSD, a free code developed by Şakar et al. [18], which allows for the calculation of radiation shielding parameters over a broad range of energies. The software is available at https://phy-x.net/PSD.

The first parameter calculated was the mass attenuation coefficient using the mixture rule (eq. 1):

$$MAC = \Sigma i\, w_i (MAC)_i \quad , \tag{1}$$

where w_i represents the weight fraction of the i-th constituent element of the absorber material and MAC_i the mass attenuation coefficient of each element of the absorber material.

After determining the MAC, the linear attenuation coefficient (eq. 2) was calculated by multiplying the MAC by the rock density (Ds). The density of the rock was obtained using the pycnometer method after macerating the rocks and passing them through a 45 μm sieve. High purity ethyl alcohol was used for the measurements. The average particle density (six samples) for the rock fragments was 2.53±0.01 g cm^{-3}.

$$MAC \times Ds = LAC \quad , \tag{2}$$

The mean free path (eq. 3) which represents the average distance a photon travels inside the material until it interacts with one of its components, the half-value layer (eq. 4) which indicates the thickness of material needed to attenuate 50% of the photons and the tenth-value layer (eq. 5) which refers to the thickness of material that attenuates 90% of the photons were calculated as:

$$MFP = \frac{1}{LAC} \quad , \tag{3}$$

$$HVL = \frac{\ln(2)}{LAC} = \frac{0.693}{LAC} \quad , \tag{4}$$

$$TVL = \frac{\ln(10)}{LAC} = \frac{2.303}{LAC} \quad , \tag{5}$$

To obtain the EBF and the EABF, the first step was to calculate the ratio (R) (eq. 6) between the partial MAC due to the Compton Effect (incoherent scattering) and the total MAC:

$$R = \frac{MAC_{Compton}}{MAC_{Total}} \quad , \tag{6}$$

The second step was to calculate the equivalent atomic number (Z_{eq}) (eq. 7) through interpolation, using the following equation:

$$Z_{eq} = \frac{Z_1(\log R_2 - \log R) + Z_2(\log R - \log R_1)}{\log R_2 - \log R_1} \quad , \tag{7}$$

where Z_1 and Z_2 represent the atomic numbers of the elements corresponding to the radii R_1 and R_2 that satisfy the inequality $R_2<R<R_1$ for photons of a given energy. The values of Z_{eq} are used in the interpolation of the G-P fitting function coefficients (a, b, c, d, and X_k) of the analyzed absorber material through the following fitting function (eq. 8):

$$P = \frac{P_1(\log Z_2 - \log Z_{eq}) + P_2(\log Z_{eq} - \log Z_1)}{\log Z_2 - \log Z_1} \quad , \tag{8}$$

 doi:10.20944/preprints202506.1819.v1

where P represents the fitting function corresponding to Z_{eq}, and P_1 and P_2 represent the fitting values for Z_1 and Z_2, respectively.

The next step was to obtain the buildup factor B as a function of the primary photon energy and the depth in MFP, for both the EBF and the EABF, starting from the G-P fitting function parameters:

$$B(E,X) = 1 + \frac{(b-1)(K^X-1)}{K-1},\ K \neq 1 \quad , \tag{9}$$

$$B(E,X) = 1 + (b-1)X,\ K = 1 \quad , \tag{10}$$

where the parameters E and X represent the primary photon energy and the penetration depth. The parameter X varies from 1 to 40 MFP and b is a fitting coefficient. The function K (eq. 11), which depends on E and X, is calculated as follows:

$$K(E,X) = cX^a + d\frac{\tanh\left(\left(\frac{X}{X_K}\right)-2\right)-\tanh(-2)}{1-\tanh(-2)},\ X \leq 40\ \text{MFP} \quad , \tag{11}$$

where a, c, and d are fitting coefficients of the G-P function, and X_k is a material-specific fitting parameter.

The results of the radiation shielding parameters between the different rock layers studied were compared based on the standard deviation of the mean. When the error bars intersected (standard deviation) it was considered that there was no significant difference (one standard deviation) in a given parameter between the rock layers.

3. Results

The results of the elemental analysis (Table 1) show that the highest amounts of silicon oxide (SiO_2) were found in the AR4 sample and the lowest in the RMPS sample, with a difference of approximately 1.1 times between them. For aluminum oxide (Al_2O_3), the highest amounts were found for sample AR1 and the lowest for sample AR4, with a difference of approximately 1.2 times between them. For iron oxide (Fe_2O_3), the highest quantities were found in the RMPS sample, while the lowest was found in the RMPP sample, with a difference of approximately 1.7 times between them. The other oxides (K_2O, SO_3, TiO_2) had concentrations of less than 2%. It is also worth mentioning that other oxides were found, but their concentrations were very low. For this reason, we decided not to present their concentrations because their contributions to the shielding parameters are negligible.

Table 1. Chemical composition (wt. %) of the sandstone samples studied.

Sample	SiO_2	Al_2O_3	Fe_2O_3	K_2O	SO_3	TiO_2
AR1	67.33±0.00	27.77±0.00	2.50±0.00	1.23±0.00	0.62±0.00	0.51±0.00
AR2	72.15±0.02	24.22±0.01	2.48±0.00	0.39±0.00	0.59±0.00	0.65±0.00
RMPS	66.56±0.01	26.69±0.02	3.94±0.00	1.75±0.00	0.73±0.00	0.54±0.00
RMPI	67.98±0.00	26.95±0.00	2.83±0.00	1.71±0.00	-	0.41±0.00
RMPP	68.48±0.01	26.30±0.01	2.37±0.01	1.74±0.00	0.64±0.00	0.48±0.00
AR4	73.23±0.01	22.53±0.01	2.60±0.00	1.14±0.00	0.43±0.00	0.48±0.00

Major oxides comprise more than 95% of the rocks chemical composition.

The mass attenuation coefficient for the lowest photon energy (0.015 MeV) was highest for RMPS (7.37 ± 0.07 cm^2/g) and lowest for AR2 (6.61 ± 0.05 cm^2/g) (Figure 3a). For the energy of 0.1 MeV (Figure 3b), RMPS (0.1738 ± 0.0001 cm^2/g) showed the highest MAC while the lowest was found for AR2 (0.1710 ± 0.0001 cm^2/g). For photons with an energy of 1.0 MeV (Figure 3c), MAC values ranged from 0.06317 ± 0.00001 cm^2/g (AR1) to 0.06371 ± 0.00001 cm^2/g (RMPP). At the highest photon energy

 doi:10.20944/preprints202506.1819.v1

analyzed (10 MeV) (Figure 3d), the lowest and highest MAC values were found for AR1 (0.02262 ± 0.00001 cm²/g) and RMPP (0.02286 ± 0.00001 cm²/g), respectively. The slight deviations observed for the lower photon energies in MAC are mainly associated with the slight variations observed in the oxide composition between repetitions for each rock sample studied.

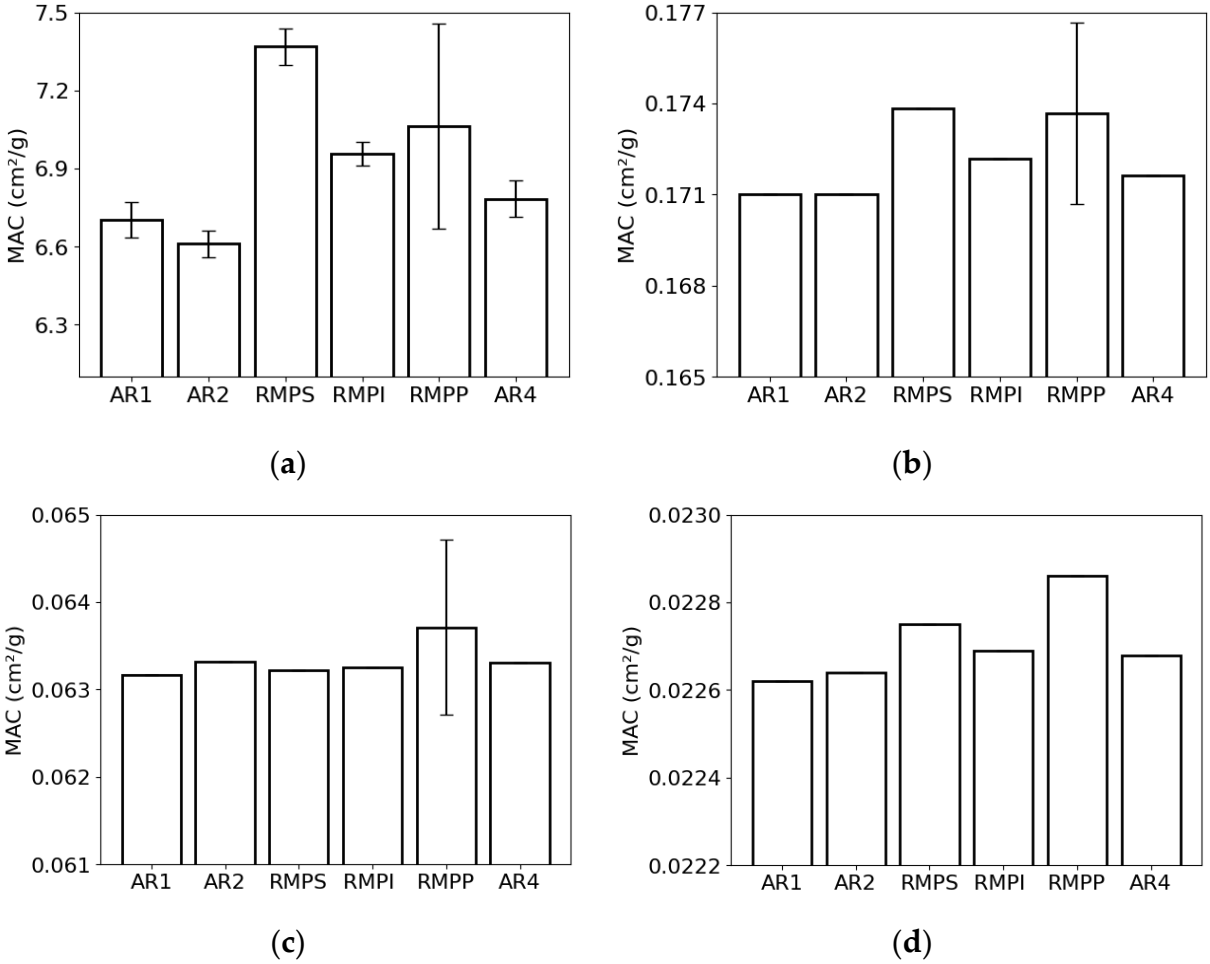

Figure 3. Mass attenuation coefficient (MAC) of the different rock samples (AR1, AR2, RMPS, RMPI, RMPP, AR4) for the following photon energies: (**a**) 0.015 MeV, (**b**) 0.1 MeV, (**c**) 1 MeV and (**d**) 10 MeV. The bars represent the standard deviation from the mean.

The linear attenuation coefficient showed similar behavior to the MAC between samples (Figure 4). This result is mainly related to the same particle density value that was adopted for all the rocks. Due to the difficulties in measuring the bulk density of the rocks, we produced a composite sample and determined the particle density for this sample. The LAC for the lowest photon energy (0.015 MeV) exhibited the greatest value for RMPS (18.7 ± 0.2 cm^{-1}) and the least for AR2 (16.7 ± 0.1 cm^{-1}) (Figure 4a). For the energy of 0.1 MeV (Figure 4b), the RMPS (0.440 ± 0.001 cm^{-1}) demonstrated the highest LAC, while the lowest was observed for AR2 (0.433 ± 0.001 cm^{-1}). For photons with an energy of 1.0 MeV (Figure 4c), the LAC values ranged from 0.1598 ± 0.0001 cm^{-1} (AR1) to 0.1612 ± 0.0001 cm^{-1} (RMPP). At the highest photon energy examined (10 MeV) (Figure 4d), the lowest and highest LAC values were observed for AR1 (0.05722 ± 0.00001 cm^{-1}) and RMPP (0.05784 ± 0.00001 cm^{-1}), respectively.

 doi:10.20944/preprints202506.1819.v1

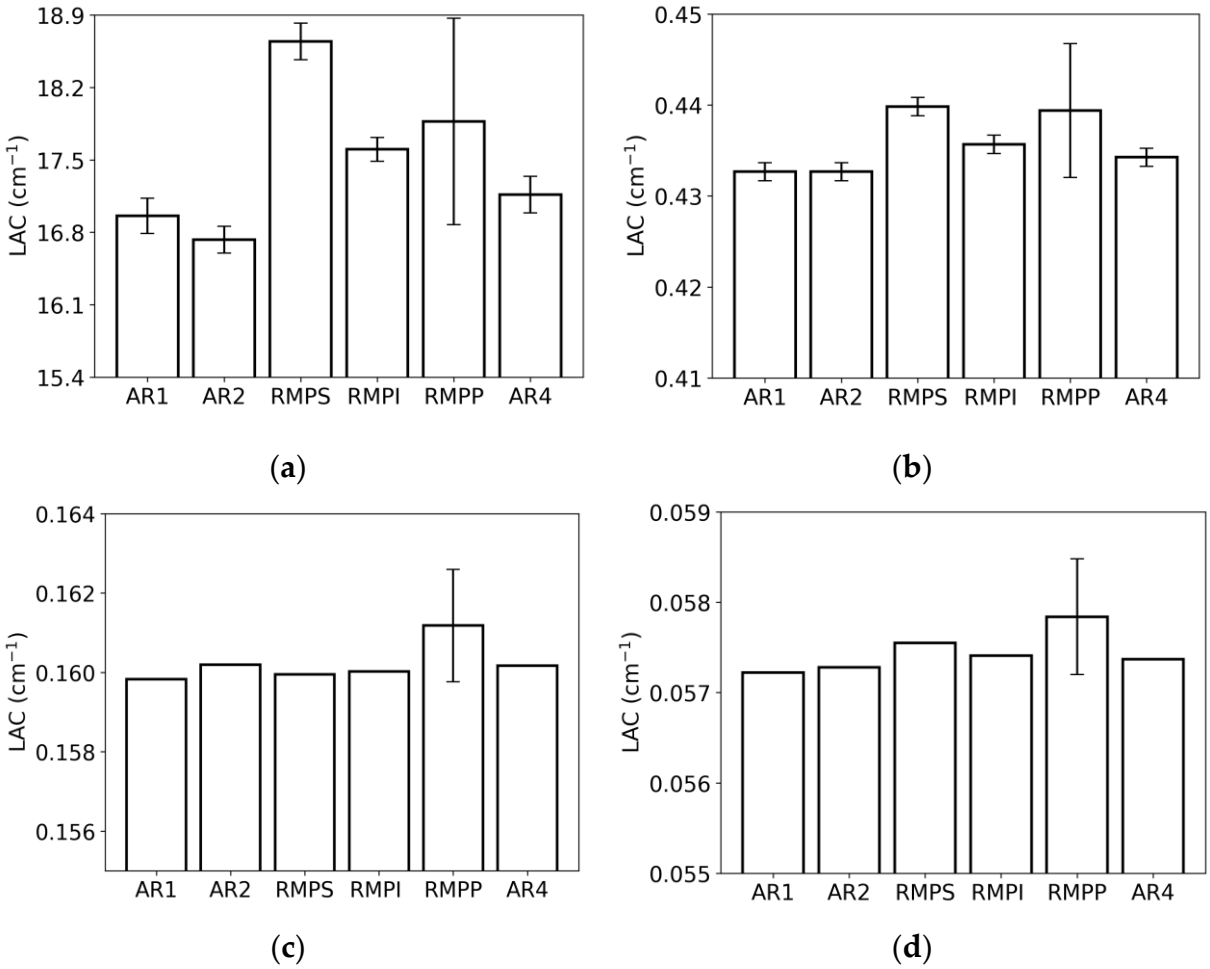

Figure 4. Linear attenuation coefficient (LAC) of the different rock samples (AR1, AR2, RMPS, RMPI, RMPP, AR4) for the following photon energies: (**a**) 0.015 MeV, (**b**) 0.1 MeV, (**c**) 1 MeV and (**d**) 10 MeV. The bars represent the standard deviation from the mean.

The lowest and highest MFP values for the lowest photon energy were observed in RMPS (0.0536 ± 0.001 cm) and AR2 (0.0598 ± 0.001 cm) (Figure 5a), respectively. For the energy of 0.1 MeV (Figure 5b), the lowest MFP value was found for RMPS (2.274 ± 0.004 cm) while the highest for AR1 (2.311 ± 0.004 cm). For the 1 MeV photons (Figure 5c), the RMPP samples (6.21 ± 0.05 cm) showed the lowest MFP values, and the AR1 samples (6.26 ± 0.01 cm) were the highest. For the highest photon energy studied (10 MeV) (Figure 5d), the lowest MFP values were found for RMPP (17.29 ± 0.19 cm) and the highest for AR1 (17.48 ± 0.03 cm).

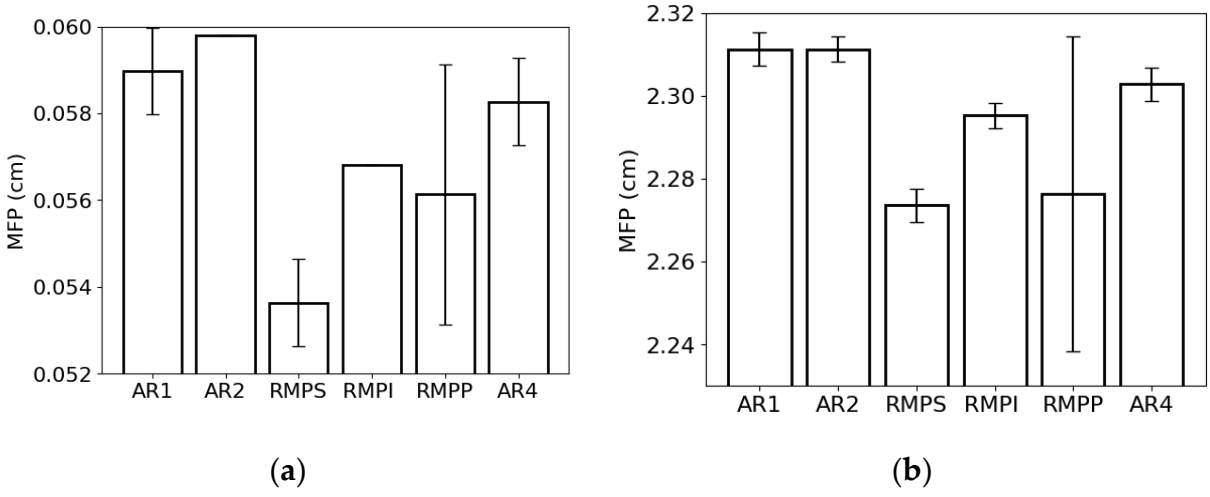

 doi:10.20944/preprints202506.1819.v1

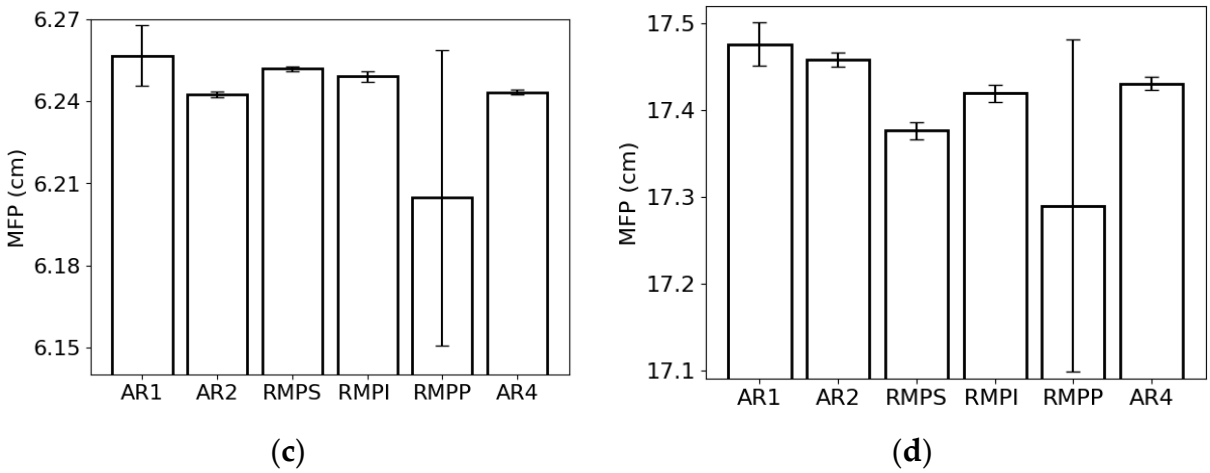

Figure 5. Mean free path (mfp) of the different rock samples for the following photon energies: (**a**) 0.015 MeV, (**b**) 0.1 MeV, (**c**) 1 MeV and (**d**) 10 MeV. The bars represent the standard deviation from the mean.

The HVL (Figure 6) followed the same trend as the MFP. This result was expected since both parameters are inversely proportional to LAC. The lowest and highest HVL values for the lowest photon energy were observed in RMPS (0.0372 ± 0.001 cm) and AR2 (0.0414 ± 0.001 cm), respectively (Figure 6a). For the energy of 0.1 MeV (Figure 6b), RMPS showed the lowest HVL value (1.576 ± 0.003 cm), while AR1 showed the highest (1.602 ± 0.002 cm). For 1 MeV photons (Figure 6c), the RMPP samples (4.30 ± 0.04 cm) had the lowest HVL values and the AR1 samples (4.34 ± 0.01 cm) had the highest. For the highest studied photon energy (10 MeV) (Figure 6d), the lowest HVL values were found for the RMPP samples (11.98 ± 0.13 cm), and the highest values were found for the AR1 samples (12.11 ± 0.02 cm).

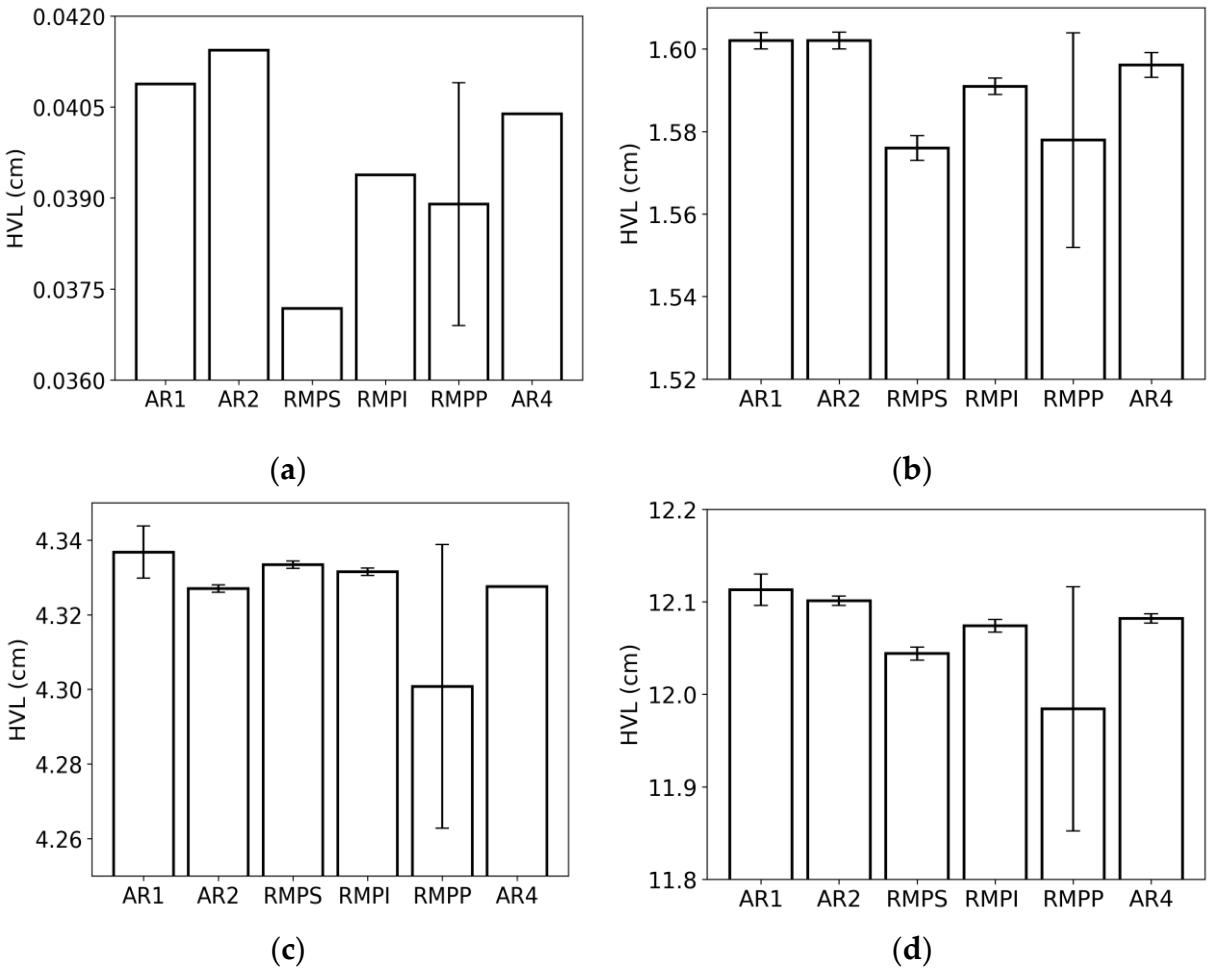

 doi:10.20944/preprints202506.1819.v1

Figure 6. Half value layer (HVL) of the different rock samples (AR1, AR2, RMPS, RMPI, RMPP, AR4) for the following photon energies: (**a**) 0.015 MeV, (**b**) 0.1 MeV, (**c**) 1 MeV and (**d**) 10 MeV. The bars represent the standard deviation from the mean.

The tenth-value layer (Figure 7) followed the same trend as HVL and MFP due to its dependence on LAC. When we analyze the lowest photon energy studied (0.015 MeV) (Figure 7a), we observe that the lowest TVL was obtained for RMPS (0.124 ± 0.001 cm) while the highest for AR2 (0.138 ± 0.001 cm), respectively. With the increment in photon energy (Figure 7b), the lowest and the highest TVL were found for RMPS (5.24 ± 0.01 cm) and AR1 (5.32 ± 0.01 cm). For the photon energy of 1 MeV (Figure 7c), the RMPP samples had the lowest TVL (14.29 ± 0.13 cm), while the highest was noticed for the AR1 samples (14.41 ± 0.02 cm). For the highest photon energy studied (Figure 7d), similar to the findings of the previous two energies, RMPP (39.8 ± 0.4 cm) presented the lowest TVL and AR1 (40.2 ± 0.1 cm) the highest, respectively.

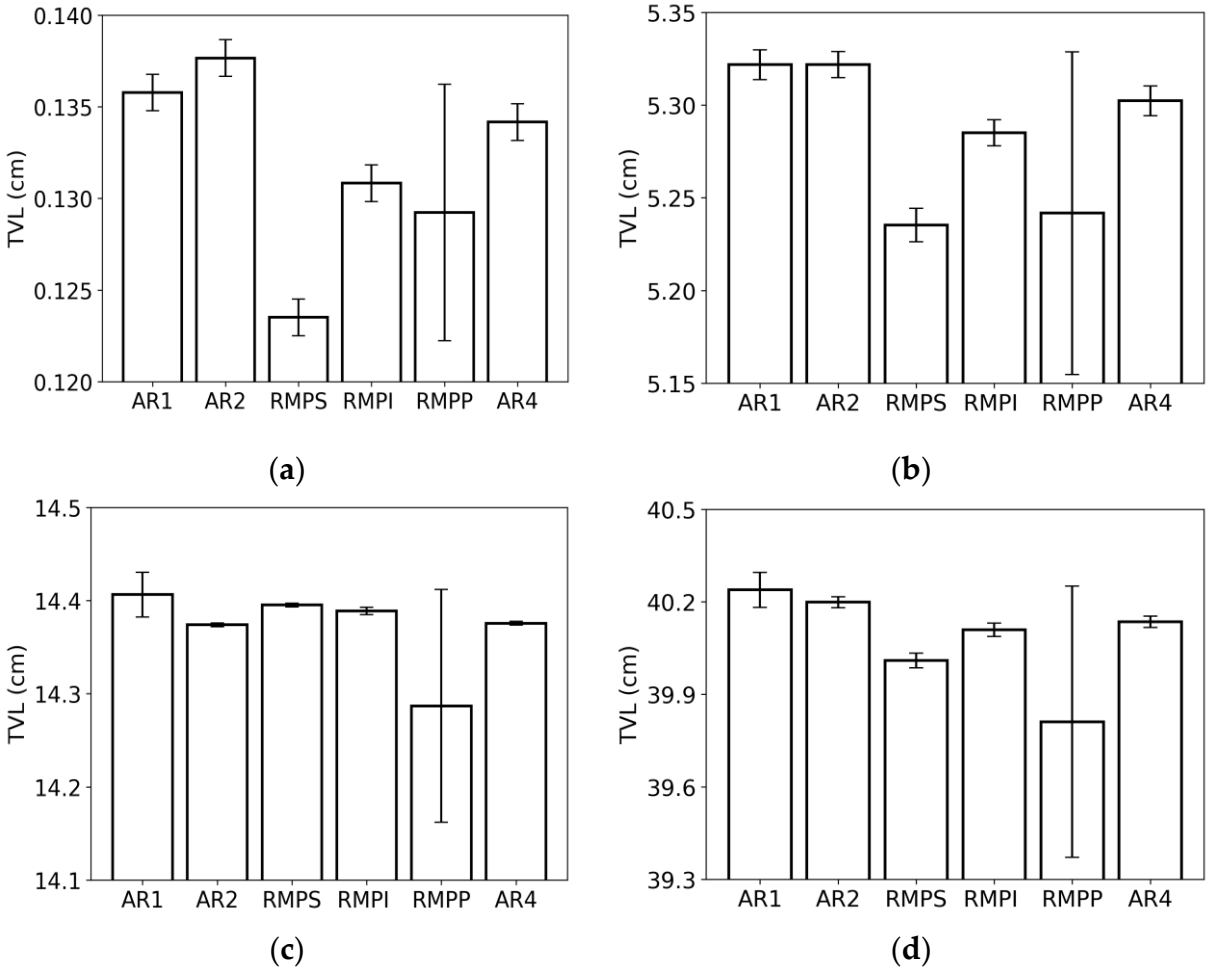

Figure 7. Tenth value layer (TVL) of the different rock samples (AR1, AR2, RMPS, RMPI, RMPP, AR4) for the following photon energies: (**a**) 0.015 MeV, (**b**) 0.1 MeV, (**c**) 1 MeV and (**d**) 10 MeV. The bars represent the standard deviation from the mean.

The EBF (Figure 8) showed similar behavior between the rock samples. The lowest values were found at the lowest (<0.1 MeV) and highest (>1 MeV) photon energies. The most significant differences were observed in the region between 0.1 and 1 MeV for the various MFP values. The increase in MFP led to an increase in EBF. This parameter was practically unaffected for 1 MFP. When comparing samples, the highest EBF values were found for AR2 (Figure 8d) with maximum values (peaks) of 2.98 ± 0.01 (1 MFP), 58.1 ± 0.6 (10 MFP), 250 ± 3 (20 MFP), 659 ± 10 (30 MFP), and 1375 ± 25 (40 MFP). The lowest values were seen for RMPS (Figure 8b), with maximum values of 2.86 ± 0.01 (1 MFP), 52.3 ± 0.5 (10 MFP), 218 ± 2 (20 MFP), 569 ± 4 (30 MFP), and 1162 ± 9 (40 MFP).

 doi:10.20944/preprints202506.1819.v1

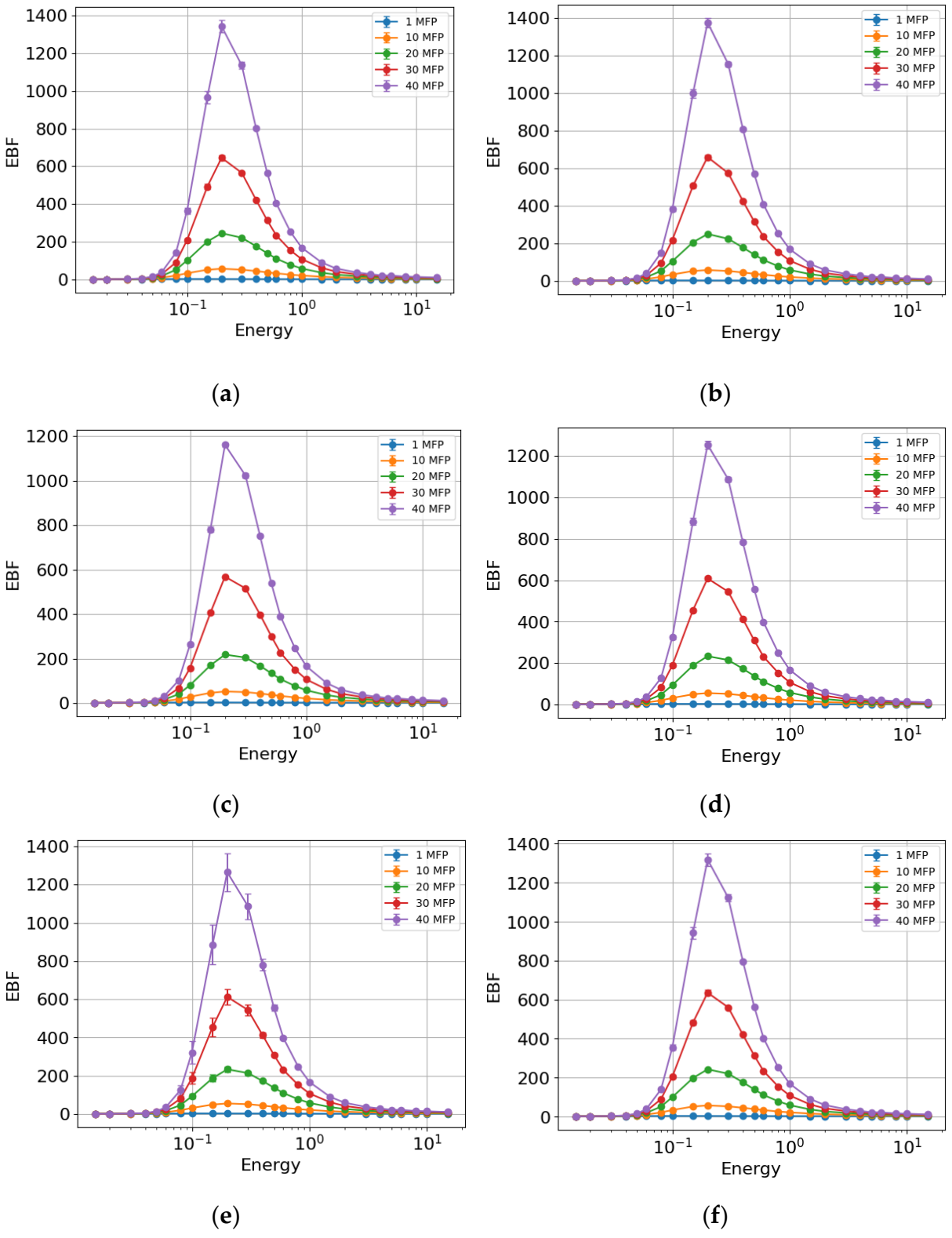

Figure 8. Energy buildup factor (EBF) of the different rock samples: (**a**) RMPP, (**b**) RMPS, (**c**) RMPI, (**d**) AR2, (**e**) AR1 and (**f**) AR4. The bars represent the standard deviation from the mean.

The EABF (Figure 9) also showed similar behavior between the rock samples. The lowest values were found at the lowest (<0.1 MeV) and highest (>1 MeV) photon energies, respectively. The most significant differences were observed in the region between 0.1 and 1 MeV for the different MFP values. With the increase in MFP, there was an increase in EABF, with this parameter being practically insensitive for 1 and 10 MFP. When comparing samples, the highest EBF values were found for AR2 (Figure 9d) with maximum values (peaks) of 4.13±0.01 (1 MFP), 101.3±0.7 (10 MFP), 442±5 (20 MFP),

 doi:10.20944/preprints202506.1819.v1

1203±16 (30 MFP) and 2526±38 (40 MFP). The lowest values were observed for RMPS (Figure 9b) with maximum values of 4.13±0.01 (1 MFP), 93.6±0.7 (10 MFP), 394±4 (20 MFP), 1037±13 (30 MFP) and 2136±30 (40 MFP).

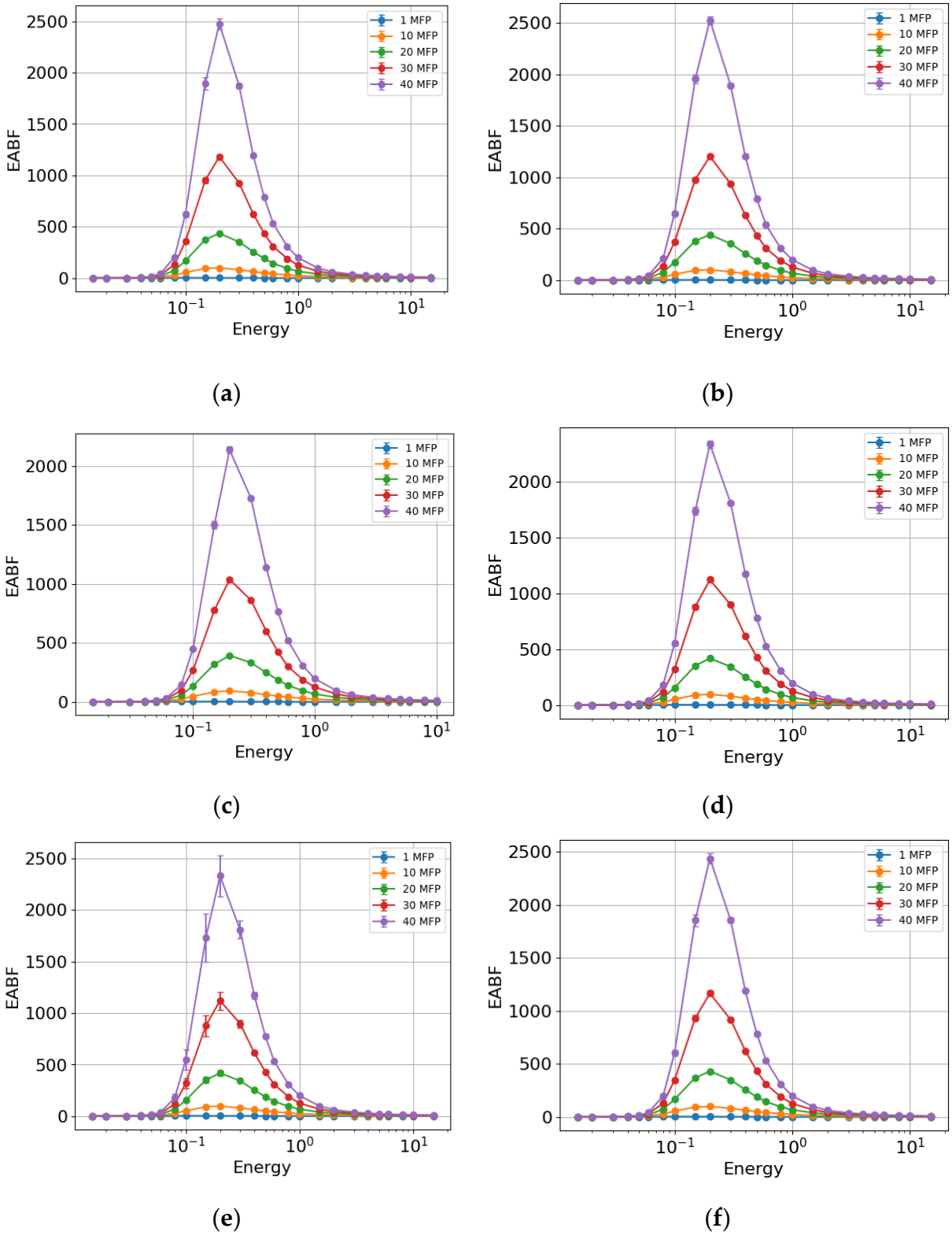

Figure 9. Exposure buildup factor (EABF) of the different rock samples: (**a**) RMPP, (**b**) RMPS, (**c**) RMPI, (**d**) AR2, (**e**) AR1 and (**f**) AR4. The bars represent the standard deviation from the mean.

4. Discussion

 doi:10.20944/preprints202506.1819.v1

The study presented here is based on the hypothesis that even minor changes in the chemical composition of rock samples can significantly impact their radiation shielding properties. In our research, we obtained the density of the sandstone from a composite sample that considered all the layers. Therefore, we decided to use a single density value for all simulations of the shielding parameters. Consequently, the differences observed among the samples are primarily influenced by their chemical composition. The density values found in our study were slightly higher than those reported by Zhou et al. [19] for sandstones, which measured 2.38 g/cm^3. In contrast, Ramos et al. [20] determined slightly higher density values of 2.65 g/cm^3 in a nearby region. The variations in density are attributed to the mineralogical composition of each sandstone studied, although this aspect was not covered in our study [21,22].

The chemical composition of the samples is primarily made up of silicon and aluminum oxides, with SiO_2 being predominant, constituting between 66% and 74% by weight. In rocks such as sandstones, a high presence of SiO_2-rich minerals like quartz is typical [22]. Other elements were also found in smaller quantities, including Fe_2O_3, K_2O, and TiO_2. Marszałek et al. [23] reported Fe_2O_3 levels ranging from 1.08% to 3.49% by weight, TiO_2 from 0.01% to 0.27%, and K_2O from 1.37% to 1.97%, which are in a similar order of magnitude to those found in our study. Additionally, the study by Shao et al. [24] indicates a predominance of SiO_2 in sandstone compositions, although the Al2O3 content they measured was nearly half of what we found in our research. Nevertheless, the values for Fe_2O_3, K_2O, and TiO_2 in their study are comparable to those observed in our findings. Other researchs on Brazilian sandstones from various formations has also yielded results consistent with ours [25,26].

The results presented in Figures 3 and 4 indicate that MAC and LAC were affected by the chemical composition of the samples. At the lowest photon energies (0.015 MeV and 0.1 MeV), the samples containing the highest amounts of Fe_2O_3, K_2O, and SO_3 (specifically RMPS and RMPP) demonstrated the greatest photon attenuation. This is attributed to the high atomic numbers of these elements compared to those found in the other samples [27,28]. In contrast, aluminum and silicon oxides had minimal impact on the rocks' attenuation. As demonstrated by Angelone et al. [29], elements such as iron possess a high capacity for photon attenuation at low energies. Medhat et al. [13] reported a positive correlation between MAC and Fe_2O_3 content, as well as an inverse relationship between MAC and SiO_2 content for photons with energy levels near 0.06 MeV. However, as photon energy increases (from 1 MeV to 10 MeV), both MAC and LAC show a decrease in photon attenuation, consistent with findings from several other studies involving rocks [6,30,31]. Another observation is the slight differences between MAC and LAC. This can be explained by the fact that, as photon energy increases, the likelihood of photons interacting with the samples decreases, rendering variations in chemical composition less significant.

The parameters of MFP (Figure 5), HVL (Figure 6), and TVL (Figure 7) exhibited the lowest values for the RMPS and RMPP samples at the lowest photon energies (0.015 MeV and 0.1 MeV). This finding aligns with the higher LAC values observed for these samples at lower energies, as MFP, HVL, and TVL are inversely related to LAC (see equations 3-5). In other words, a higher LAC in a sample results in a shorter distance that photons can travel, along with the necessary thicknesses to attenuate 50% and 90% of the radiation [32]. As photon energy increases from 1 to 10 MeV, the differences between these parameters become less pronounced, with the lowest values noted for the RMPP samples, which also display the highest variability. Abd El-Azeem and Harpy [33] reported HVL, LAC, and MAC values similar to those found in our study for sandstones at photon energies near 0.1 MeV and 1 MeV. Their sandstone samples contain higher amounts of SiO_2 and Fe_2O_3 compared to our samples. The LAC and TVL values observed in our study are comparable to those reported by Jaha et al. [34] for concrete samples at energies around 1 MeV, as concrete is a commonly used material for radiation shielding. Additionally, at approximately the same photon energy of 1 MeV, Khan et al. [35], who studied rocks from the Jabal Elham mountain, found LAC, MFP, HVL, and TVL values similar to those in our research. This indicates that the sandstones we investigated share attenuation characteristics with other rock types.

 doi:10.20944/preprints202506.1819.v1

The greater sensitivity of the shielding parameters (LAC, MAC, MFP, HVL, and TVL) to the chemical composition of the samples at lower photon energies (0.015 MeV and 0.1 MeV) is associated with the process responsible for attenuating the photons. At lower energies, the most important process is photoelectric absorption, which is dependent on Z^{4-5} [36–38]. For this reason, slight variations in the chemical composition of the samples, particularly in the heavier elements, have a greater impact on the shielding parameters [39]. For energies where incoherent scattering becomes the primary interaction mechanism (E > 0.1 MeV), the rock chemical composition becomes less significant [40]. This effect has only a linear dependence on Z [37,41,42]. At 10 MeV, the shielding parameters again show greater differences between samples but are still less profound than observed in the smallest photon energies. This result is mainly associated with the production of pairs that begins to occur for photons greater than 1.02 MeV [43]. This effect is dependent on Z^2 [36,37], which explains why the shielding parameters become more sensitive to the chemical composition of the samples again [27].

Both EBF and EABF (Figure 7 and Figure 8) demonstrate a clear dependence on the energy of the incident photons. In both low- and high-energy regions, the accumulation factors are at their lowest. This trend is linked to the predominant interaction mechanisms, such as the photoelectric effect and pair production [44]. In the low-energy range, where photoelectric absorption is most pronounced, the number of photons that are completely absorbed or removed is maximized. Consequently, photons are absorbed quickly [45]. This results in EBF and EABF values being close to one, indicating minimal scattering and no buildup [46]. In contrast, in intermediate energy regions where incoherent scattering is more significant, photons continue to interact with the material after their initial interaction. This leads to higher accumulation factors [47]. Multiple incoherent scattering events occur, which increase the EBF and EABF values [46]. Moreover, accumulation factors are affected by the depth of photon penetration. The deeper a photon penetrates the material, the lower the likelihood of significant interaction, resulting in reduced accumulation factors [48].

Karabul et al. [49], working with basaltic rocks, showed EBF and EABF similar to those observed in our study, with peaks in the region between 0.1 and 0.4 MeV. These authors mention that the low effective atomic number of the rocks (not shown in our study) increases EBF and EABF due to the longer interaction time of the photons with the sample. Bantan et al. [50], also working with basaltic rocks, showed lower EBF and EABF values than those found in our study, especially for higher MFP. The differences in the content of iron and aluminum oxides between the samples of these authors and ours explain the differences in the results. In work by Rashwan et al. [51] on granitoid, the EBF and EABF values were similar to those in our study. However, the samples analyzed by these authors had higher amounts of SiO2 and lower amounts of Al2O3 compared to our study but with similar Fe2O3 values. The influence of elements such as Fe2O3 on EBF is evident in the study by Elsafi et al. [46]. These authors analyzed rocks without the presence of this oxide, showing EBF values 3 to 4 times lower than those found for the sandstones we studied.

In general, we observed that the heavier elements have a greater influence on the shielding parameters (MAC, LAC, MFP, HVL, and TVL), especially for the lower photon energies. This result shows that even slight differences in the chemical composition of the samples influence the shielding parameters, confirming our hypothesis. The Fe_2O_3 content between the highest and lowest concentrations found in the rocks was approximately 1.6 times. In the case of K_2O, this difference was approximately 4.5 times, although the concentration of this oxide was much lower than the major ones. Thus, for the lowest photon energies (0.015 MeV and 0.1 MeV), the RMPS samples represent the material with the highest shielding capacity and AR2 the lowest. As the photon energy increases, the RMPP samples show the best results and AR1 the worst. The increased energy of the photons means that thicker layers of material are needed to shield the photons [52–54]. Considering the lowest (0.015 MeV) and highest (10 MeV) photon energy analyzed and the most suitable shielding materials, we found that approximately 0.04 cm of material shields 50% of the photons and approximately 0.12 cm shields 90% for the first case and in the second case approximately 11.9 cm (HVL) and approximately 39.8 cm (TVL), respectively. Thus, 40 cm layers of sandstone are capable of shielding

 doi:10.20944/preprints202506.1819.v1

almost all of the photons considered to be high energy. When considering EBF and EABF, we found the best shielding results for the RMPS sample. The lower values of these parameters indicate better shielding performance, lower buildup, and greater photon absorption by the sample. This finding means that people are less exposed to scattered photons.

5. Conclusions

Our results indicate that even minor variations in the composition of sandstone oxides, particularly those with higher atomic numbers such as Fe_2O_3, significantly affect the shielding properties of these rocks. Generally, samples containing larger quantities of heavier elements exhibited higher mass and linear attenuation coefficients. As a result, these samples required reduced material thicknesses (mean free path, half-value layer, and tenth-value layer) to effectively attenuate photons across various energy levels. In the intermediate energy range (around 1 MeV), where incoherent scattering is the primary mechanism for photon attenuation, the differences between samples were relatively minor, despite variations in their chemical composition. However, at the highest photon energy (10 MeV), the samples displayed more pronounced variations in shielding parameters, largely due to the pair production effect.

Parameters related to photon scattering, such as EBF and EABF, demonstrated optimal shielding characteristics in samples composed of heavier elements. Overall, our findings suggest that the sandstone samples studied possess good shielding capabilities. Although different samples from various rock layers showed some variability in their shielding effectiveness, all layers provided adequate shielding results. Therefore, this study indicates that sandstone samples can be utilized in their natural state, or that material can be extracted from the rocks to produce blocks or be mixed with other substances, such as concrete, to create more efficient photon attenuation materials.

Author Contributions: Conceptualization, L.F.P. and I.S.M.; methodology, G.P. and I.S.M.; formal analysis, G.P.; investigation, G.P.; resources, L.F.P. and I.S.M.; writing – original draft, G.P. and L.F.P., writing – review and editing, G.P and L.F.P., project administration, I.S.M. and L.F.P.; funding acquisition, L.F.P. All authors have read and agree to the published version of the manuscript.

Funding: This research was partially funded by "Conselho Nacional de Desenvolvimento Científico e Tecnológico" (CNPQ) (Grant 303950/2023-4) and "Coordenação de Aperfeiçoamento de Pessoal de Nível Superior" (Capes) (Grant Code 001).

Institutional Review Board Statement: Not applicable.

Informed Consent Statement: Not applicable.

Data Availability Statement: All data are available upon reasonable request to gabywpietralla@gmail.com.

Acknowledgments: We thank FASCA (Laboratory of Physics Applied to Soils and Environmental Sciences) for the infrastructure for the XRF analyses.

Conflicts of Interest: The authors declare no conflicts of interest.

References

1. Arif Sazali, M.; Alang Md Rashid, N.K.; Hamzah, K. A Review on Multilayer Radiation Shielding. *IOP Conference Series: Materials Science and Engineering* **2019**, *555*, 012008.
2. More, C. V., Alsayed, Z., Badawi, M. S., Thabet, A. A., & Pawar, P. P.. Polymeric composite materials for radiation shielding: a review. *Environmental chemistry letters* **2021**, *19*, 2057-2090.
3. Onaizi, A. M., Amran, M., Tang, W., Betoush, N., Alhassan, M., Rashid, R. S., Onaizi, S. A.. Radiation-shielding concrete: A review of materials, performance, and the impact of radiation on concrete properties. *Journal of Building Engineering* **2024**, *97*, 110800.

 doi:10.20944/preprints202506.1819.v1

4. Abdo, A. E. S., Ali, M. A. M., & Ismail, M. R.. Natural fibre high-density polyethylene and lead oxide composites for radiation shielding. *Radiation Physics and Chemistry* **2003**, *66(3)*, 185-195.
5. Pioro, L. S., Sadovskiy, B. F., & Pioro, I. L.. Research and development of a high-efficiency one-stage melting converter-burial-bunker method for vitrification of high-level radioactive wastes. *Nuclear engineering and design* **2001**, *205(1-2)*, 133-144.
6. Al-Buriahi, M. S., Sayyed, M. I., Bantan, R. A., & Al-Hadeethi, Y.. Nuclear radiation shielding characteristics of some natural rocks by using EPICS2017 library. *Materials* **2021**, *14(16)*, 4669.
7. Masoud, M.A.; El-Khayatt, A.M.; Shahien, M.G.; Bakhit, B.R.; Suliman, I.I.; Zayed, A.M. Radiation Attenuation Assessment of Serpentinite Rocks from a Geological Perspective. *Toxics* **2022**, *10*, 697–697.
8. Ding, B.; Zhang, L.; Liu, J. Study on Shielding and Radiation Resistance of Basalt Fiber to Gamma Ray. *Materials* **2022**, 15, 2522.
9. Abdullah, M.A.H.; Rashid, R.S.M.; Amran, M.; Hejazii, F.; Azreen, N.M.; Fediuk, R.; Voo, Y.L.; Vatin, N.I.; Idris, M.I. Recent Trends in Advanced Radiation Shielding Concrete for Construction of Facilities: Materials and Properties. *Polymers* **2022**, *14*, 2830.
10. Badarloo, B.; Lehner, P.; Bakhtiari Doost, R. Mechanical Properties and Gamma Radiation Transmission Rate of Heavyweight Concrete Containing Barite Aggregates. *Materials* **2022**, *15*, 2173.
11. Mansouri, E.; Mesbahi, A.; Malekzadeh, R.; Mansouri, A. Shielding Characteristics of Nanocomposites for Protection against X- and Gamma Rays in Medical Applications: Effect of Particle Size, Photon Energy and Nano-Particle Concentration. *Radiation and Environmental Biophysics* **2020**, *59*, 583–600.
12. Çelen, Y.Y.; Akkurt, I.; Ceylan, Y.; Atçeken, H. Application of Experiment and Simulation to Estimate Radiation Shielding Capacity of Various Rocks. *Arabian Journal of Geosciences* **2021**, *14*.
13. Medhat, M.E.; Demir, N.; Akar Tarim, U.; Gurler, O. Calculation of Gamma-Ray Mass Attenuation Coefficients of Some Egyptian Soil Samples Using Monte Carlo Methods. *Radiation Effects and Defects in Solids* **2014**, *169*, 706–714.
14. Akman, F.; Kaçal, M.R.; Sayyed, M.I.; Karataş, H.A. Study of Gamma Radiation Attenuation Properties of Some Selected Ternary Alloys. *Journal of Alloys and Compounds* **2019**, *782*, 315–322.
15. Sayyed, M.I.; AlZaatreh, M.Y.; Dong, M.G.; Zaid, M.H.M.; Matori, K.A.; Tekin, H.O. A Comprehensive Study of the Energy Absorption and Exposure Buildup Factors of Different Bricks for Gamma-Rays Shielding. *Results in Physics* **2017**, *7*, 2528–2533.
16. Vesely, F.F.; Delgado, D.; Spisila, A.L.; Brumatti, M. Divisão Litoestratigráfica Do Grupo Itararé No Estado Do Paraná. *Boletim Paranaense de Geociências* **2021**, *78*.
17. Meneguzzo, I.S.; Pontes H.S.; Ribeiro, A.G.. Classificação e fatores condicionantes dos movimentos de massa em taludes de corte na BR 277- Balsa Nova, Paraná. *Revista SODEBRAS* **2023**, *18*, 39-45.
18. Şakar, E.; Özpolat, Ö.F.; Alım, B.; Sayyed, M.I.; Kurudirek, M. Phy-X / PSD: Development of a User Friendly Online Software for Calculation of Parameters Relevant to Radiation Shielding and Dosimetry. *Radiation Physics and Chemistry* **2020**, *166*, 108496.
19. Zhou, Z.; Cai, X.; Chen, L.; Cao, W.; Zhao, Y.; Wei, L. Influence of Cyclic Wetting and Drying on Physical and Dynamic Compressive Properties of Sandstone. *Engineering Geology* **2017**, *220*, 1–12.
20. Ramos, P. F. O., Stael, G. C., Azeredo, R. B., Ade, M. V. B., Bergamaschi, S., Lourenço, J., & Bermudez, S. L. B.. Petrographic and Petrophysical Characterization of Sandstones from Rio Bonito Formation, Paraná Basin (Southern Brazil). *Anais da Academia Brasileira de Ciências* **2024**, *96(4)*, e20240365.
21. Hurst, A.; Archer, J.S. Sandstone Reservoir Description: An Overview of the Role of Geology and Mineralogy. *Clay Minerals* **1986**, *21*, 791–809.
22. He, W.; Chen, K.; Hayatdavoudi, A.; Sawant, K.; Lomas, M. Effects of Clay Content, Cement and Mineral Composition Characteristics on Sandstone Rock Strength and Deformability Behaviors. *Journal of Petroleum Science and Engineering* **2019**, *176*, 962–969.
23. Marszałek, M.; Alexandrowicz, Z.; Rzepa, G. Composition of Weathering Crusts on Sandstones from Natural Outcrops and Architectonic Elements in an Urban Environment. *Environmental Science and Pollution Research International* **2014**, *21*, 14023–14036.

 doi:10.20944/preprints202506.1819.v1

24. Shao, L.; Stattegger, K.; Garbe-Schoenberg, C.-D. . Sandstone Petrology and Geochemistry of the Turpan Basin (NW China): Implications for the Tectonic Evolution of a Continental Basin. *Journal of Sedimentary Research* **2001**, *71*, 37–49.
25. Montibeller, C.C.; Rafael, G.; Zanardo, A.; Rohn, R.; Roveri, C.D. Geochemistry of Siltstones from the Permian Corumbataí Formation from the Paraná Basin(State of São Paulo, Brazil): Insights of Provenance, Tectonic and Climatic Settings. *Journal of South American Earth Sciences* **2020**, *102*, 102582–102582.
26. Corrêa, J. C., Cavallaro, F. A., Garcia, R. H., Santos, R. S., Amade, R. A., da Silva Bernardes, T. L., Hamada, M. M.. Chemical and physical analysis of sandstone rock from Botucatu formation. *Brazilian Journal of Radiation Sciences* **2021**, *9*(1A).
27. Akkurt, I.; Mavi, B.; Akkurt, A.; Basyigit, C.; Kilincarslan, S.; Yalim, H.A. Study on Dependence of Partial and Total Mass Attenuation Coefficients. *Journal of Quantitative Spectroscopy and Radiative Transfer* **2005**, *94*, 379–385.
28. Şen Baykal, D.; Tekin, H.O.; Çakirli Mutlu, R.B. An Investigation on Radiation Shielding Properties of Borosilicate Glass Systems. *International Journal of Computational and Experimental Science and Engineering* **2021**, *7*, 99–108.
29. Angelone, M.; Bubba, T.A.; Esposito, A. Measurement of the Mass Attenuation Coefficient for Elemental Materials in the Range 6⩽Z⩽82 Using X-Rays from 13 up to 50 Kev. *Applied Radiation and Isotopes* **2001**, *55*, 505–511.
30. Han, I.; Demir, L.; Şahin, M. Determination of Mass Attenuation Coefficients, Effective Atomic and Electron Numbers for Some Natural Minerals. *Radiation Physics and Chemistry* **2009**, *78*, 760–764.
31. Obaid, S.S.; Sayyed, M.I.; Gaikwad, D.K.; Pawar, Pravina.P. Attenuation Coefficients and Exposure Buildup Factor of Some Rocks for Gamma Ray Shielding Applications. *Radiation Physics and Chemistry* **2018**, *148*, 86–94.
32. Sayyed, M.I.; Issa, S.A.M.; Auda, S.H. Assessment of Radio-Protective Properties of Some Anti-Inflammatory Drugs. *Progress in Nuclear Energy* **2017**, *100*, 297–308.
33. Abd El-Azeem, S.A.; Harpy, N.M. Radioactive Attenuation Using Different Types of Natural Rocks. *Materials* **2024**, *17*, 3462–3462.
34. Jaha, N.; Islam, G.S.; Kabir, M.F.; Khandaker, M.U.; Chowdhury, F.-U.-Z.; Bhuian, A.S.I. Ionizing Radiation Shielding Efficacy of Common Mortar and Concrete Used in Bangladeshi Dwellings. *Case Studies in Construction Materials* **2022**, *17*, e01547.
35. Khan, A.; Al alhareth, A.; Mobark, S.; Al-Mahri, W.; Sharyah, N.A.; Zmanan, S.A.; Albargi, H.B.; Abdalla, A.M. Experimental and Theoretical Investigations of the γ-Rays Shielding Performance of Rock Samples from Najran Region. *Annals of Nuclear Energy* **2023**, *183*, 109676–109676.
36. Singh, M.; Mudahar, G.S. Energy Dependence of Total Photon Attenuation Coefficients of Composite Materials. *International Journal of Radiation Applications and Instrumentation. Part A. Applied Radiation and Isotopes* **2002**, *43*, 907–911.
37. Appoloni, C.R.; Rios, E.A. Mass Attenuation Coefficients of Brazilian Soils in the Range 10–1450 KeV. *Applied Radiation and Isotopes* **1994**, *45*, 287–291.
38. Şensoy, A.T.; Gökçe, H.S. Simulation and Optimization of Gamma-Ray Linear Attenuation Coefficients of Barite Concrete Shields. *Construction and Building Materials* **2020**, *253*, 119218.
39. Pires, L.F. Radiation Shielding Properties of Weathered Soils: Influence of the Chemical Composition and Granulometric Fractions. *Nuclear Engineering and Technology* **2022**, *54*, 3470–3477.
40. Kaky, K.M.; Sayyed, M.I. The Radiation Shielding Parameters of a Standard Silica Glass System. *Silicon* **2023**, *16*.
41. Singh, C.; Singh, T.; Kumar, A.; Mudahar, G.S. Energy and Chemical Composition Dependence of Mass Attenuation Coefficients of Building Materials. *Annals of Nuclear Energy* **2004**, *31*, 1199–1205.
42. Singh, V.; Badiger, N. Investigation on Radiation Shielding Parameters of Ordinary, Heavy and Super Heavy Concretes. *Nuclear Technology and Radiation Protection* **2014**, *29*, 149–156.
43. Issa, S.A.M.; Rashad, M.; Hanafy, T.A.; Saddeek, Y.B. Experimental Investigations on Elastic and Radiation Shielding Parameters of WO3-B2O3-TeO2 Glasses. *Journal of Non-Crystalline Solids* **2020**, *544*, 120207.

 doi:10.20944/preprints202506.1819.v1

44. Büyükyıldız, M.; Kılıç, A.D.; Yılmaz, D. White and Some Colored Marbles as Alternative Radiation Shielding Materials for Applications. *Radiation effects and defects in solids* **2020**, *175*, 657–671.
45. Issa, S.A.M.; Sayyed, M.I.; Kurudirek, M. Study of Gamma Radiation Shielding Properties of TeO_2ZnO - TeO_2 Glasses. *Bulletin of Materials Science* **2017**, *40*, 841–857.
46. Elsafi, M.; Alrashedi, M.F.; Sayyed, M.I.; Al-Hamarneh, I.F.; El-Nahal, M.A.; El-Khatib, M.; Khandaker, M.U.; Osman, H.; Askary, A.E. The Potentials of Egyptian and Indian Granites for Protection of Ionizing Radiation. *Materials* **2021**, *14*, 3928.
47. Lakshminarayana, G.; Baki, S.O.; Kaky, K.M.; Sayyed, M.I.; Tekin, H.O.; Lira, A.; Kityk, I.V.; Mahdi, M.A. Investigation of Structural, Thermal Properties and Shielding Parameters for Multicomponent Borate Glasses for Gamma and Neutron Radiation Shielding Applications. *Journal of Non-Crystalline Solids* **2017**, *471*, 222–237.
48. Sayyed, M.I.; Lakshminarayana, G.; Kityk, I.V.; Mahdi, M.A. Evaluation of Shielding Parameters for Heavy Metal Fluoride Based Tellurite-Rich Glasses for Gamma Ray Shielding Applications. *Radiation Physics and Chemistry* **2017**, *139*, 33–39.
49. Karabul, Y.; Amon Susam, L.; İçelli, O.; Eyecioğlu, Ö. Computation of EABF and EBF for Basalt Rock Samples. *Nuclear Instruments and Methods in Physics Research Section A: Accelerators, Spectrometers, Detectors and Associated Equipment* **2015**, *797*, 29–36.
50. Bantan, R.A.R.; Sayyed, M.I.; Mahmoud, K.A.; Al-Hadeethi, Y. Application of Experimental Measurements, Monte Carlo Simulation and Theoretical Calculation to Estimate the Gamma Ray Shielding Capacity of Various Natural Rocks. *Progress in Nuclear Energy* **2020**, *126*, 103405.
51. Rashwan, M.A.; Abdelwahab, W.; Azer, M.K.; Zakaly, H.M.H.; Alarifi, S.S.; Ene, A.; Thabet, I.A. Physico-Mechanical Properties and Shielding Efficiency in Relation to Mineralogical and Geochemical Compositions of Um Had Granitoid, Central Eastern Desert, Egypt. *Frontiers in Earth Science* **2023**, *11*.
52. Karpuz, N. Radiation Shielding Properties of Glass Composition. *Journal of Radiation Research and Applied Sciences* **2023**, *16*, 100689–100689.
53. Camargo, M.A.; Kodum, K.S.; Pires, L.F. How does the soil chemical composition affect the mass attenuation coefficient? A study using computer simulation to understand the radiation-soil interaction processes. *Brazilian Journal of Physics* **2021**, *51(6)*, 1775-1783.
54. Costa, J.C.; Borges, J.A.R.; Pires, L.F.; Arthur, R.C.J.; Bacchi, O.O.S. Soil mass attenuation coefficient: Analysis and evaluation. *Annals of Nuclear Energy* **2014**, *64*, 206-211.